IOP Publishing Phys. Med. Biol. 65 (2020) 055013 (12pp) https://doi.org/10.1088/1361-6560/ab6f97

Physics in Medicine & Biology

IPEM Institute of Physics and Engineering in Medicine

PAPER

Simulation study to improve the performance of a whole-body PbF_2 Cherenkov TOF-PET scanner

RECEIVED
30 June 2019

REVISED
20 January 2020

ACCEPTED FOR PUBLICATION
24 January 2020

PUBLISHED
6 March 2020

Dania Consuegra[1,4], Samo Korpar[1,2], Peter Križan[1,3], Rok Pestotnik[1], Gašper Razdevšek[3] and Rok Dolenec[1,3]

[1] Jožef Stefan Institute, Ljubljana, Slovenia
[2] Faculty of Chemistry and Chemical Engineering, University of Maribor, Maribor, Slovenia
[3] Faculty of Mathematics and Physics, University of Ljubljana, Ljubljana, Slovenia
[4] Author to whom any correspondence should be addressed.

E-mail: dania.consuegra@ijs.si

Keywords: positron emission tomography, Cherenkov radiation, lead fluoride, silicon photomultipliers, multi-layer detector

Abstract

Using Cherenkov radiation in positron emission tomography (PET) has the potential to improve the time of flight (TOF) resolution and reduce the cost of detectors. In previous studies promising TOF results were achieved when lead fluoride (PbF_2) crystals were used instead of a scintillator. In this work, a whole-body PbF_2 Cherenkov TOF-PET scanner was simulated and optimized. Different configurations of the PbF_2 crystals and their surface treatment were considered. Also evaluated was the influence of the crystal-photodetector coupling and of the detection efficiency of the photodetectors. Of special interest is a whole-body PbF_2 Cherenkov TOF-PET scanner with a multi-layer detector, which improves the time resolution and reduces the parallax error, without compromising the detection efficiency. Images of a phantom were reconstructed for different configurations of the simulated whole-body PbF_2 Cherenkov TOF-PET scanner and the quality of images was compared to that of a whole-body TOF-PET scanner with standard LSO scintillators. The TOF resolution of the whole-body PbF_2 Cherenkov TOF-PET scanner with a multi-layer detector was 143 ps FWHM, out of which the fundamental limitation due to light production and transportation was only 22 ps FWHM.

1. Introduction

Positron emission tomography (PET) is a powerful nuclear medicine imaging technique widely used nowadays in oncology, neuropsychiatry and cardiology. It is based on detection of two gamma rays with an energy of 511 keV originating from the point of annihilation of the positron emitted by a radio-pharmaceutical. The gamma-ray detectors in a PET device are installed in the form of a ring around the investigated tissue; the two gamma rays get detected, defining a line of response (LOR) on which the annihilation point lies. From a large number of LORs the distribution of the radiotracer in the body can be reconstructed, giving a three-dimensional image of the observed intensity of a physiological process. The contrast of imaging with a PET device can be improved by increasing the number of detected pairs or reducing the background fluctuations. The former can be increased by improving coincidence detection efficiency, while the latter can be reduced by the time of flight (TOF) measurement.

1.1. Improving the efficiency

Standard whole-body PET scanners have an axial length of about 20 cm and can only use a fraction of the activity in the body. This fraction may be increased by extending the axial length of the device. This is associated with increased detector surface area and a significant increase in its price, which in turn, is largely determined by the cost of the scintillator. The development of devices for imaging of the total-body is one of the hottest trends in functional and molecular imaging due to the shorter required imaging time and/or the reduction of the activity of the injected radio-pharmaceutical (Cherry *et al* 2018). This reduces the incidence of images blurred by patient movement and results in images with more details and less radiation exposure. The approach reflects the current

trend in medicine: to develop systems-based treatments and more individualized care. The reduction of the dose per scan to less than 0.2 mSv is potentially opening a broader use of PET in sensitive populations such as children, allowing up to 40 scans of a subject receiving the same effective dose as currently received in a single scan (Badawi *et al* 2019).

1.2. Improving the TOF resolution

In standard whole-body PET scanners, contribution to noise is uniform along the line of response since the annihilation point position along this line is not known. This location can be determined by measuring the time difference between the times when two gamma rays are detected with sufficient timing precision (Tomitani 1981). If we want to determine the annihilation point position with an accuracy of 1 cm, we have to measure the time difference with an accuracy of 66 ps. Standard whole-body TOF-PET scanners currently reaching clinical practice have the TOF resolution between 300 and 400 ps, which already significantly improves the contrast in large object imaging (Hsu *et al* 2017, Vereos Digital PET/CT Performance whitepaper 2019). One of the latest commercial entries is the Siemens Healthineers Biograph Vision PET/CT with a TOF resolution of 214 ps. It uses LSO crystals in combination with silicon photomultipliers rather than the conventional photomultiplier tubes (Siemens Biograph Vision Technical Sheet 2019). With the present state of fast light sensors and read-out electronics, the main limitation in the time resolution is given by the scintillator crystal that typically requires about 100 ps (ter Weele *et al* 2014) to reach a maximum light output and then, decreases exponentially with a decay time on the order of 10 ns (Conti *et al* 2009). Pushing the limits of the TOF-PET resolution improves the contrast of the images, resulting in a corresponding clinical sensitivity increase and a dose reduction potential.

1.3. Using Cherenkov light for TOF-PET

In order to develop better devices, it is necessary to explore new ways of prompt light production, in which, as soon as the gamma ray interacts in the detector, photons are emitted. One possibility is to use Cherenkov light emitted by electrons moving with velocities exceeding the speed of light in the chosen radiator material. In PET such fast electrons are produced due to photoelectric effect or Compton scattering of the 511 keV gamma rays.

The use of Cherenkov light to detect gamma rays in PET was first discussed by Ooba *et al* (2004), where it was proposed to improve the time resolution by using a Cherenkov light produced in a silica aerogel with a refractive index of 1.2. Unfortunately, such a radiator would have very small yield because of its very low density. Another group that also carried out measurements of the time resolution by using lead glass and microchannel plate photomultiplier tubes (MCP-PMT) reported 170 ps for the coincidence time resolution, which was already a better result than what was achieved with scintillation crystals of comparable size (Miyata *et al* 2006). With a low signal detection threshold and two un-doped LuAG crystals, a 250 ps TOF was obtained for a small amount of prompt Cherenkov photons (Lecoq *et al* 2010). On the other hand, lead fluoride (PbF_2) crystal does not scintillate and is, therefore, a pure Cherenkov photon emitter. Using PbF_2 crystals of 15 mm length and MCP-PMT as light sensors a TOF resolution of 95 ps was demonstrated (Korpar *et al* 2011). The TOF was also studied using PbF_2 crystals and silicon photomultiplier (SiPM) as photodetector (Dolenec *et al* 2016), where the best result obtained for TOF resolution was 297 ps. This even improved to 190 ps using single-cell hits but at the expense of lower efficiency. Such promising experimental results using PbF_2 Cherenkov radiator in combination with SiPMs leaves space for further studies on the topic. Also, previous work has shown that the surface treatment of the crystals and the properties of photodetectors used have an important influence on the performance of Cherenkov TOF-PET scanners. In Alokhina *et al* (2018) a whole-body PbF_2 Cherenkov TOF-PET scanner was simulated using GATE/Geant4. With diffuse white coating for the crystal surfaces, a TOF resolution of 180 ps was obtained. While the promptly produced Cherenkov photons enable excellent accuracy of the time measurement, the travel time spread of photons inside crystals of sufficient length for PET application represents a fundamental limitation for the TOF resolution. One possibility to improve the timing without affecting gamma stopping power is to use a multi-layer detector arrangement. Here, the crystal is separated in multiple layers, each having its own photodetector. In this way the travel time spread of photons inside each layer is reduced, while the total thickness of the material, used to absorb the gamma energy, can remain the same.

In this work the effects of different crystal surface treatments and photodetector parameters are studied using the simulation of a whole-body PbF_2 Cherenkov TOF-PET scanner. The possibility to obtain better timing information using a multi-layer detector arrangement was explored by simulating a detector composed of three 5 mm thick layers instead of a single, 15 mm long crystal. This paper is organized as follows: the parameters used in the simulations are presented in section 2. In section 3 the obtained results for the whole-body PbF_2 Cherenkov TOF-PET scanners are shown. In section 4 the results are discussed and compared with the results obtained for the whole-body LSO TOF-PET scanner. Finally, conclusions are given in section 5.

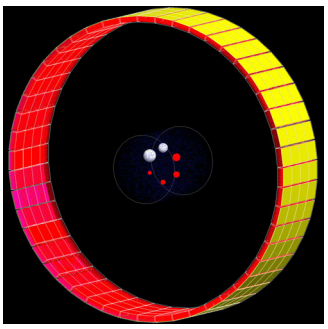

Figure 1. A 4-ring whole-body TOF-PET scanner simulated in this study, as visualized by the GATE software. Also shown is the simulated phantom.

2. Methods

2.1. Whole-body TOF-PET scanner

A whole-body TOF-PET scanner simulation was developed using GATE software (Strul *et al* 2003). The geometric characteristics of the simulated scanner are shown in figure 1. The geometry consists of four rings, each with 48 detector blocks of dimensions $54 \times 54 \times 24\,mm^3$. Each block is a (13×13) matrix of LSO or PbF_2 crystals. There is a gap of 0.01 mm between the crystals inside the same block and a gap of 1.89 mm between crystals from different blocks. The axial length is approximately 22 cm and the diameter is approximately 86 cm. Different lengths of crystals from 3 to 30 mm were investigated. Their cross-section was $4 \times 4\,mm^2$. To each crystal a 1 mm thick block of SiO_2, representing the photodetector material, was attached. The photodetectors were tested with an ideal (100%) photon detection efficiency (PDE) as well as with a realistic PDE of a SiPM (Hamamatsu Catalogue 2018). The effect of the optical interface between the crystal and the photodetector sensitive surface was investigated by adding a 0.1 mm thick quartz block in between, representing the window of a realistic photodetector. As the first step of this study, simulations were carried out using a point source. Once the optimal crystal length, taking into account a reasonable compromise between coincidence detection efficiency and TOF resolution, was established, a Jaszczak phantom with two cold and four hot spheres and radius of 100 mm was simulated. The diameters for cold spheres were 37 mm and 28 mm while for the hot spheres the diameters were 22 mm, 17 mm, 13 mm and 10 mm. The activity concentration inside the hot spheres was three times larger than the phantom background.

Different types of crystal optical surfaces were simulated, referred throughout this article as *spike*, *diffuse*, *bare* and *black*. The Geant4 (Allison *et al* 2016) UNIFIED model was used in order to simulate each optical surface as a *'polishedbackpainted'* surface. The cases of *spike* optical surface and *diffuse* optical surface represent two extremes of possible parameters for the simulated optical surfaces, the first acting as a mirror with 95% reflectivity and the second as a completely diffuse reflector, isotropically reflecting 95% of the photons reaching it. The 5% that was not reflected for each case is absorbed in the corresponding optical surface. When *bare* and *black* surfaces were used, all the optical photons that exited the crystal were stopped. However, the difference was in the refractive index used for the definition of the *'polishedbackpainted'* optical surface, which was 1.0 for the *bare*, *spike* and *diffuse* optical surfaces and 1.5 for the *black* optical surface. For *black* optical surface, there are less total reflections inside the crystal and direct events, which carry better timing information, gain more weight.

Another crucial parameter is the time response of the detector. For the whole-body LSO TOF-PET scanner the timing was defined by GATE as the gamma interaction time. Additionally, a time resolution of 150 ps was included in the GATE simulation, taking into account the contributions of the scintillation light production mechanisms, time spread due to light propagation in the crystal, photodetector resolution and electronics. This resulted in a TOF resolution of 223 ps, which matches the resolution of the whole-body LSO TOF-PET scanners currently available. For the whole-body PbF_2 Cherenkov TOF-PET scanners most of the results shown include no additional contributions beyond the first detected photon travel time spread in the crystals, as an ideal photodetector time resolution was presumed in the GATE simulation, to investigate the best case for the whole-body PbF_2 Cherenkov TOF-PET scanners. Optimistically, SiPM photodetectors suitable for Cherenkov TOF-PET could soon reach at least 100 ps time resolution. The effect of such time resolution was also explored by including it in some of the results shown.

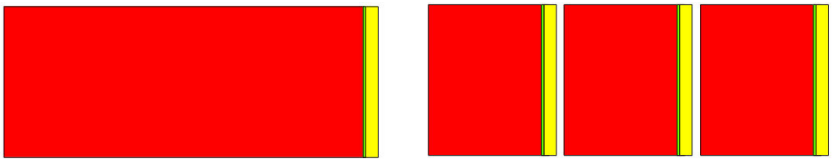

Figure 2. Schematic representation of the two annihilation gamma detector geometries simulated in this study: a single 15 mm long PbF_2 crystal read out with a SiPM (left) and a triplet of 5 mm long PbF_2 crystals read out with SiPMs (right).

2.2. Whole-body PbF_2 Cherenkov TOF-PET scanner with a multi-layer detector

Another geometry was also simulated, a whole-body PbF_2 Cherenkov TOF-PET scanner with a multi-layer detector (figure 2). In this geometry instead of using a single PbF_2 crystal of 15 mm length, three crystals of 5 mm length, with the corresponding photodetectors, were used. The layers were separated by a space of 0.5 mm. As it was done with the whole-body PbF_2 Cherenkov TOF-PET scanner, first the behavior of the TOF resolution was tested using a point source and then, the quality of the obtained images was evaluated using the phantom. For the whole-body PbF_2 Cherenkov TOF-PET scanner with a multi-layer detector only the *diffuse* and *black* optical surfaces were used. For this multi-layer geometry, we must take into account that the coincidences can also be detected by the detectors of different layers. For instance, the coincidence can happen between the detectors in the first layer on both sides of the ring, between the detectors in the first layer on one side and the third layer on the other side of the ring, or any other possible combination. This was corrected by taking into account the delays in detection time of gamma originating in the center, estimated for all possible combinations of layers. Such correction is only precise for objects in the center of the field of view, while some deterioration is expected outside of the center. This can be corrected with a more involved channel-to-channel calibration, not attempted here.

2.3. Analysis of the simulated data

For different surface treatments and lengths of the crystals, the figure of merit (FOM) was calculated as:

$$FOM = \frac{N_{Coincidences}}{FWHM_{TOF}},$$

were $N_{Coincidences}$ is the number of coincidences for $6 \cdot 10^6$ primary events and the $FWHM_{TOF}$ is the time of flight resolution. The latter was obtained by fitting the central part of the coincidence timing distribution with a sum of two Gaussian functions, and estimating the full width at half maximum (FWHM) of the fit function. Such FOM was chosen since the signal to noise ratio is proportionally related to the $N_{Coincidences}$ and $1/FWHM_{TOF}$ (Budinger 1983, Conti *et al* 2009). A correlation between these two parameters was already used as FOM to compare the TOF-PET performance of scintillators (Conti *et al* 2009). The FOM was used to find the optimal length of the crystals for the whole-body PbF_2 Cherenkov TOF-PET scanner. Once this was found, the effects of taking into account the realistic crystal-photodetector optical interface and using a realistic PDE of the SiPM, were investigated.

With the optimized parameters of the whole-body PbF_2 Cherenkov TOF-PET scanner, also the phantom was simulated. The images were reconstructed using the most likely position (MLP) method (Vandenberghe and Karp 2006). All reconstructed images of the phantom were corrected for attenuation and were obtained with $3 \cdot 10^8$ primary events simulated. Such statistics correspond to approximately 7.5 s of a realistic PET acquisition for the injected activity of 300 MBq. The quality of reconstructed images was compared in terms of their contrast to noise ratio (CNR). This is defined as:

$$CNR = \frac{C_s - C_b}{\sigma_b},$$

where C_s is the average of the counts per pixel at the location of the sphere of interest, C_b is the average of the counts per pixel corresponding to the phantom background and σ_b is the fluctuation (RMS) of the phantom background counts. The C_s was calculated taking into account the contribution of the partial pixels on the edges of the sphere of interest. It has been shown that in order for an object to be detectable in the image, CNR must be greater than 3–5 (Cherry *et al* 2003). Important to point out is that the CNR was calculated using one slice of 1 cm thickness centered on the hot spheres. The estimate of standard deviation of CNR was based on the statistics of the total count rate inside the sphere of interest and the number of reconstructed image pixels contributing. Compared to this, the uncertainty due to the background count rate, estimated over a much larger area, was negligible.

The quality of reconstructed images was also compared in terms of their percent contrast ($Q_{H,j}$) and percent background variability (N_j) following a procedure exactly like the one used for the National Electrical Manufactures Association (NEMA) standard, except that 30 background regions of interest (ROIs) were used instead of

60, since the phantom simulated in this study is smaller than the one used by NEMA standard. Five different slices for the estimation of the background per each hot sphere (j), were used. In each slice, six ROIs per each hot sphere were drawn. The average of the counts in the pixels ($C_{B,j}$) over the 30 ROIs for the background per each hot sphere was recorded. The values of $Q_{H,j}$ and the N_j were calculated using the central slice and four other 1 cm thick slices that are ± 1 cm and ± 2 cm on either sides of the central one.

The percent contrast for each hot sphere j was calculated as:

$$Q_{H,j} = \frac{C_{H,j}/C_{B,j} - 1}{a_H/a_B - 1} * 100\%,$$

where $C_{H,j}$ is the average counts per pixel for the sphere of interest j, a_H is the activity concentration in the hot sphere and a_B is the activity concentration in the phantom background.

The percent background variability for the sphere j was calculated as:

$$N_j = \frac{SD_j}{C_{B,j}} * 100\%,$$

where SD_j is the standard deviation of the average of the counts per 30 background regions of interest, corresponding to the sphere of interest j, calculated as:

$$SD_j = \sqrt{\sum_{k=1}^{K} (C_{B,j,k} - C_{B,j})^2/(K-1)}, K = 30,$$

were $C_{B,j,k}$ is the average of the counts per pixel in ROI k.

The $C_{H,j}$ and $C_{B,j,k}$ were calculated taking into account the contribution of the partial pixels on the edges of the spheres of interest. To correct the partial pixel effect, the number of counts inside the pixels was weighted with the fraction of pixel surface inside the ROI and added to the estimated counts inside the ROI.

Two full-reference quality metrics, the root mean square error (RMSE) and the structural similarity index (SSIM) (Wang *et al* 2004), were also used to compare the quality of the reconstructed images. The reference image was generated using a Monte-Carlo simulation of the same phantom geometry and activity concentrations as used in the full GATE simulation. The RMSE and SSIM for the reconstructed images were calculated using the MATLAB 2018b software *immse* and *ssim* functions, respectively, with default parameters. The RMSE values were evaluated for the whole images, while the SSIM values are reported as the average of the SSIM over the region corresponding to each individual hot sphere.

3. Results

3.1. Whole-body TOF-PET scanner

In figure 3 the results are shown for the FOM as a function of the length of the crystal. For these simulations a whole-body PbF_2 Cherenkov TOF-PET scanner geometry was used, just with the PbF_2 crystals and the photodetectors with an ideal PDE. Also, four different types of optical surfaces treatments for the crystals were tested. The length of 15 mm was selected for the PbF_2 crystal as the optimal for whole-body PbF_2 Cherenkov TOF-PET scanner. The differences in the general behavior of the FOMs obtained with different optical surfaces, are small. However, for the *black* optical surface the detection efficiency is lower by approximately 30%. With this *black* optical surface treatment just the direct Cherenkov photons and those that underwent a total reflection from the crystal surfaces are being detected. In that sense, a better TOF is expected but at the expense of lower efficiency.

For the whole-body PbF_2 Cherenkov TOF-PET scanner with 15 mm long crystals, the influence of including the detection loss due to the realistic interface between the crystal and the photodetector was tested in combination with the ideal and realistic PDE. In tables 1 and 2 the results obtained for the TOF and the coincidence detection efficiency for each optical surface are shown. Introducing the realistic crystal-photodetector interface into the simulation, while keeping an ideal PDE, slightly improved the TOF resolution and decreased the coincidence detection efficiency; this is due to the photons totally reflected from the interface back to the crystal, that would have otherwise already reached the photodetector. As expected, the realistic PDE reduces the coincidence detection efficiency further and worsens the TOF resolution. This is because the probability to detect any direct photons is reduced and in a larger fraction of events the timing is defined by one of the photons that are reflected from the surfaces, and can have a long travel time inside the crystal.

In figure 4 the TOF distributions for the whole-body PbF_2 Cherenkov TOF-PET scanner using 15 mm crystal length for *diffuse* and *black* optical surface, respectively, are shown. These timing results were obtained with the simulation that included the realistic interface and realistic PDE. When *diffuse* optical surface treatment was used, random reflections on the optical surfaces appear. These random reflections from the wrapping of the

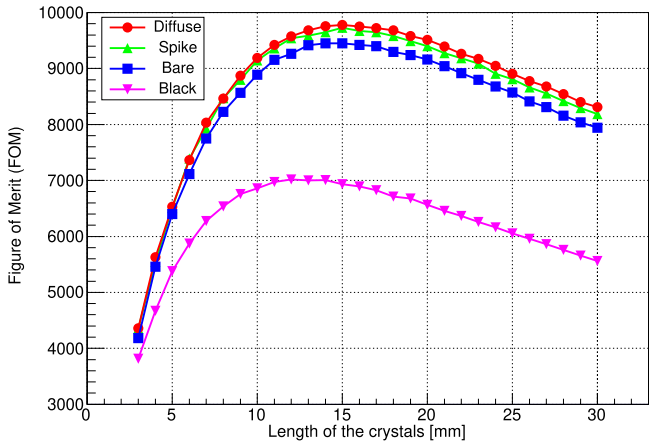

Figure 3. FOMs for different lengths of the crystals for a whole-body PbF_2 Cherenkov TOF-PET scanner with *diffuse*, *spike*, *bare* and *black* optical surface treatments in red, green, blue and magenta, respectively.

Table 1. TOF resolution for whole-body PbF_2 Cherenkov TOF-PET scanner, for different optical surface treatments.

Detector configuration	*Spike*	*Diffuse*	*Bare*	*Black*
PbF_2 + interface (ideal) + PDE (ideal)	69 ps	68 ps	68 ps	59 ps
PbF_2 + interface (realistic) + PDE (ideal)	65 ps	68 ps	65 ps	59 ps
PbF_2 + interface (realistic) + PDE (realistic)	83 ps	94 ps	82 ps	61 ps

Table 2. Coincidence detection efficiency for whole-body PbF_2 Cherenkov TOF-PET scanner, for different optical surface treatments. The coincidence detection efficiency is the $N_{Coincidences}$ divided by the primary events of the simulation.

Detector configuration	*Spike*	*Diffuse*	*Bare*	*Black*
PbF_2 + interface (ideal) + PDE (ideal)	11%	11%	11%	6.8%
PbF_2 + interface (realistic) + PDE (ideal)	10%	11%	9.8%	6.7%
PbF_2 + interface (realistic) + PDE (realistic)	4.3%	5.7%	4.0%	1.5%

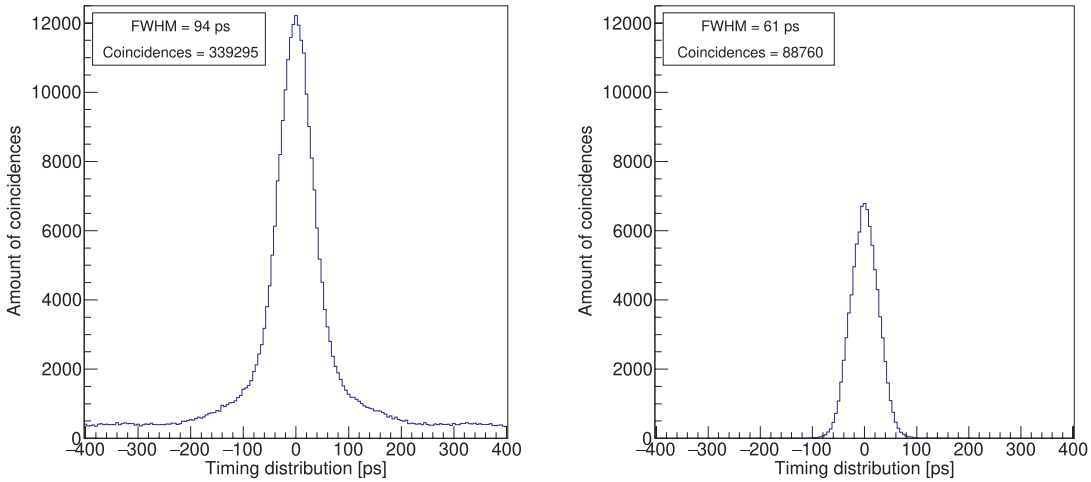

Figure 4. TOF distributions for the whole-body PbF_2 Cherenkov TOF-PET scanners, using point source for *diffuse* optical surface (left) and *black* optical surface (right).

crystals are visible as the tails of the TOF distribution shown in figure 4, degrading the images, as we shall discuss in what follows.

The results shown so far were obtained using a point source. In figure 5 the reconstructed images of the simulated phantom are shown for two cases: the whole-body PbF_2 Cherenkov TOF-PET scanner, using *diffuse* optical surface, and *black* optical surface. When using the *diffuse* optical surface a better coincidence detection efficiency is achieved, however, the quality of reconstructed image using the *black* surface is visibly better due to more accurate TOF determination, despite the lower number of coincidences detected. This is the effect of the long tails in TOF distribution.

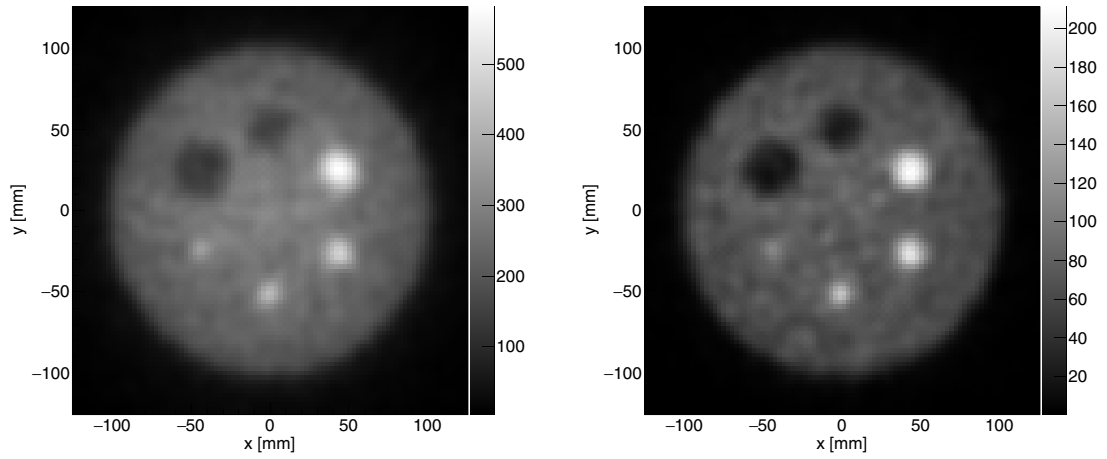

Figure 5. Reconstructed phantom images for the whole-body PbF_2 Cherenkov TOF-PET scanners, for *diffuse* optical surface (left) and *black* optical surface (right).

3.2. Whole-body PbF_2 Cherenkov TOF-PET scanner with a multi-layer detector

The whole-body PbF_2 Cherenkov TOF-PET scanner with a multi-layer detector was tested as an alternative geometry that could improve the timing results and the quality of reconstructed images even further. In figure 6 the TOF distributions for the whole-body PbF_2 Cherenkov TOF-PET scanner with a multi-layer detector are shown, using a point source for the two most interesting optical surface treatments, *diffuse* and *black*. The TOF resolution improved to 22 ps in the case of *black* optical surface. Also the detection efficiency improved due to better light collection of the shorter crystals. These results indicate that the main limitation remaining are the photodetectors and any improvement in their timing can be advantageous for TOF-PET. The TOF is similar for the multi-layer geometry with *diffuse* optical surface treatment because it is dominated in both cases by the narrowest part of the TOF distribution. This is due to the contribution of direct Cherenkov photons detected in the SiPMs. However, for the reconstructed images, the contribution of the random reflections in the crystal, that generate the tails in TOF distribution when the *diffuse* optical surface treatment is used, also became important. This is visible in figure 7, showing the reconstructed images of the phantom when simulating the whole-body PbF_2 Cherenkov TOF-PET scanner with a multi-layer detector geometry. When a time spread of 100 ps for the photodetector was included in the simulation, the whole-body PbF_2 Cherenkov TOF-PET scanners performance worsened, but still remained better than that of the whole-body LSO TOF-PET scanner. These results are shown in table 3.

3.3. Quantitative analysis of image quality

The reconstructed images for each TOF-PET geometry were investigated more quantitatively by estimating the CNR for the four hot spheres, shown in figure 8. It is possible to observe that by using the whole-body PbF_2 Cherenkov TOF-PET scanners with *black* optical surface treatment, higher values of CNR were obtained with respect to the whole-body PbF_2 Cherenkov TOF-PET scanners with *diffuse* optical surface treatment. Figure 8 (right) shows how the CNR for each whole-body PbF_2 Cherenkov TOF-PET scanner simulated changes when a 100 ps of time spread for the SiPMs is incorporated. These results for the CNR are compared with the ones obtained for the whole-body LSO TOF-PET scanner with a crystal length of 20 mm.

In tables 4 and 5 the results obtained for the CNR of hot spheres for each optical surface treatment with and without time spread of the SiPMs are shown. Taking into account the results obtained for the whole-body LSO TOF-PET scanner also simulated in this study, very competitive results for the whole-body Cherenkov TOF-PET scanners were obtained even when the 100 ps time spread of the SiPMs was used.

In tables 6 and 7 the results obtained for the NEMA percent contrast and percent background variability for the whole-body Cherenkov TOF-PET scanners, with and without time spread of the SiPMs, are shown. In table 8 the results obtained for the percent contrast and percent background variability for the whole-body LSO TOF-PET scanner simulated are shown. Also for these quantitative indicators, very competitive results for the whole-body Cherenkov TOF-PET scanners were achieved.

Image quality comparisons in terms of RMSE (lower value is better) and SSIM (higher value is better) are summarized in tables 9 and 10. The results are in agreement with other image quality metrics presented above.

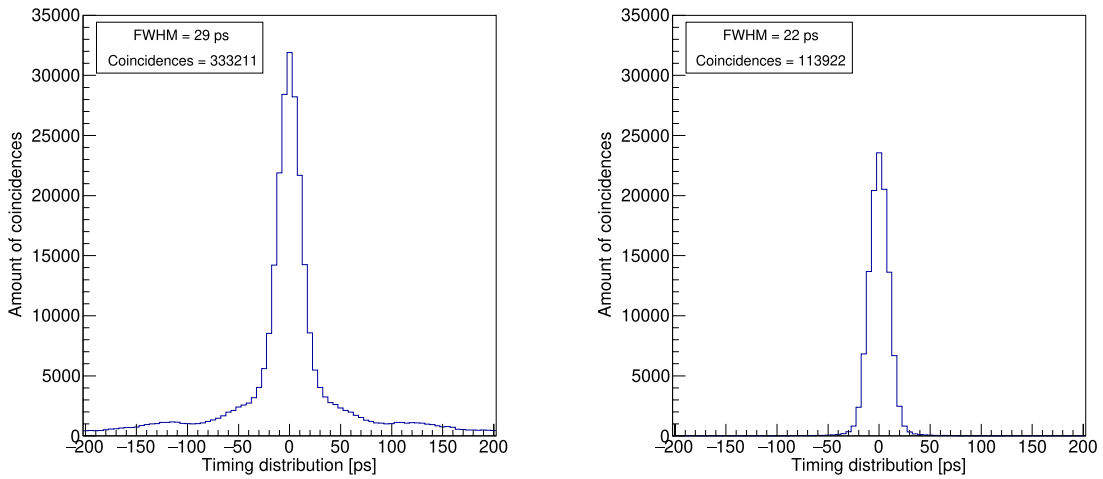

Figure 6. TOF distributions for the whole-body PbF_2 Cherenkov TOF-PET scanners with a multi-layer detector, using point source for *diffuse* optical surface (left) and *black* optical surface (right).

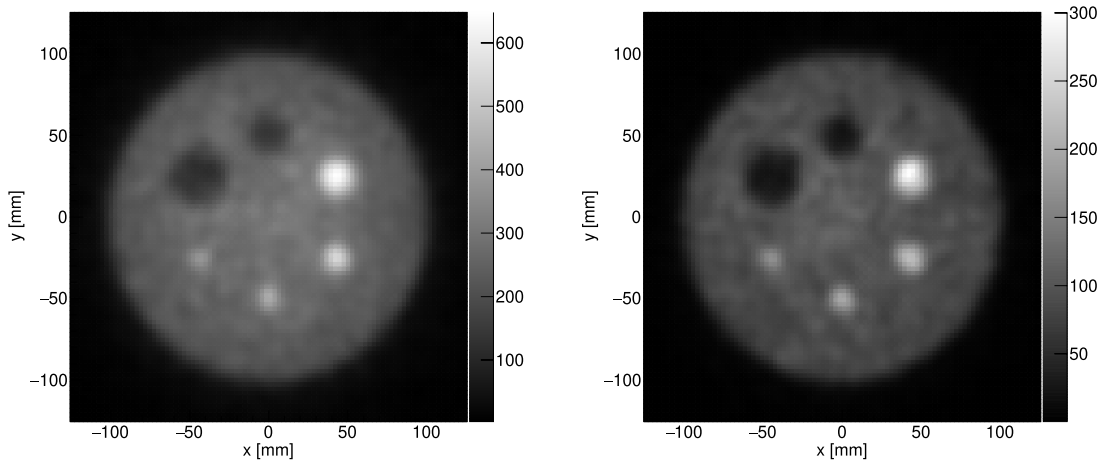

Figure 7. Reconstructed phantom images for the whole-body PbF_2 Cherenkov TOF-PET scanners with a multi-layer detector, for *diffuse* optical surface (left) and *black* optical surface (right).

Table 3. TOF for the whole-body PbF_2 Cherenkov TOF-PET scanners, for different geometries and optical surface treatments with and without 100 ps of time spread for the SiPMs. TOF for the whole-body LSO TOF-PET scanner with time resolution of 150 ps included in the simulation is also shown.

	Time of flight (TOF)			
Simulation conditions	*Black*	*Diffuse*	*BlackML*	*DiffuseML*
Without SiPM time spread	61 ps	94 ps	22 ps	29 ps
With 100 ps of SiPM time spread	154 ps	196 ps	143 ps	164 ps
	Time of flight (TOF)			
Whole-body LSO TOF-PET scanner	223 ps			

4. Discussion

Different configurations of a possible whole-body PbF_2 Cherenkov TOF-PET scanner were simulated and compared to the whole-body LSO TOF-PET scanner performance also simulated in this study. For the PbF_2 crystals, a length of 15 mm was selected as a reasonable compromise between TOF resolution, coincidence detection efficiency and gamma stopping power. As expected, including realistic crystal-photodetector coupling and PDE in the simulation resulted in worse coincidence detection efficiency and TOF resolution. When a time spread of 100 ps for the SiPMs was also included, it became the dominant factor limiting the TOF resolution. Most of the simulations were preformed for two crystal optical surface treatments, *diffuse* and *black*, since these are the two optical surfaces most easily achieved when preparing crystal arrays for use in the experiment. With

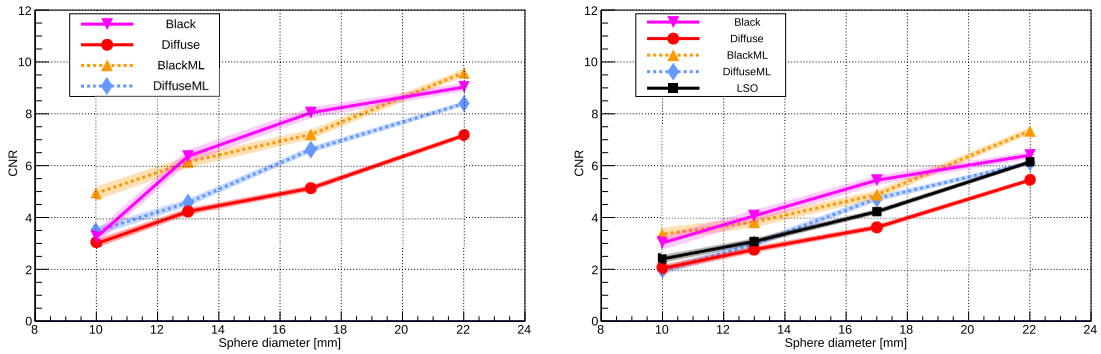

Figure 8. CNR of the four hot spheres, for each whole-body TOF-PET geometry simulated, without time spread for the SiPMs (left) and with 100 ps time spread for the SiPMs (right). ML stands for the multi-layer detector geometry. Estimated standard deviations of the CNR values are shown as error bands for each graph.

Table 4. Contrast to noise ratio of hot spheres for each optical surface treatment for the whole-body PbF_2 Cherenkov TOF-PET scanners without time spread of the SiPMs.

	Contrast to noise ratio (CNR)			
Sphere Size	*Black*	*Diffuse*	*BlackML*	*DiffuseML*
10 mm	3.3 ± 0.3	3.1 ± 0.2	5.0 ± 0.3	3.5 ± 0.2
13 mm	6.4 ± 0.3	4.3 ± 0.1	6.2 ± 0.2	4.6 ± 0.1
17 mm	8.1 ± 0.2	5.2 ± 0.1	7.2 ± 0.2	6.6 ± 0.1
22 mm	9.0 ± 0.2	7.2 ± 0.1	9.6 ± 0.1	8.4 ± 0.1

Table 5. Contrast to noise ratio of hot spheres for each optical surface treatment for the whole-body PbF_2 Cherenkov TOF-PET scanners with 100 ps time spread for the SiPMs and for the whole-body LSO TOF-PET scanner with time resolution of 150 ps included.

	Contrast to noise ratio (CNR)				
Sphere Size	LSO	*Black*	*Diffuse*	*BlackML*	*DiffuseML*
10 mm	2.4 ± 0.2	3.1 ± 0.3	2.1 ± 0.1	3.4 ± 0.2	2.0 ± 0.2
13 mm	3.1 ± 0.1	4.1 ± 0.2	2.8 ± 0.1	3.9 ± 0.2	3.0 ± 0.1
17 mm	4.3 ± 0.1	5.5 ± 0.2	3.7 ± 0.1	4.9 ± 0.2	4.8 ± 0.1
22 mm	6.2 ± 0.1	6.4 ± 0.1	5.5 ± 0.1	7.3 ± 0.1	6.1 ± 0.1

Table 6. Percent contrast and percent background variability for each optical surface treatment for the whole-body PbF_2 Cherenkov TOF-PET scanners without time spread of the SiPMs.

	Percent contrast ($Q_{H,j}$) (%)				Percent background variability (N_j) (%)			
Sphere Size	*Black*	*Diffuse*	*BlackML*	*DiffuseML*	*Black*	*Diffuse*	*BlackML*	*DiffuseML*
10 mm	39.4	34.6	53.8	35.6	11.1	8.3	10.9	7.8
13 mm	68.0	44.7	64.0	42.6	10.1	8.0	10.2	7.5
17 mm	83.4	52.0	71.8	57.9	9.2	7.8	9.3	7.2
22 mm	94.1	70.0	95.0	73.1	8.5	7.8	8.5	7.0

Table 7. Percent contrast and percent background variability for each optical surface treatment for the whole-body PbF_2 Cherenkov TOF-PET scanners with 100 ps time spread for the SiPMs.

	Percent contrast ($Q_{H,j}$) (%)				Percent background variability (N_j) (%)			
Sphere Size	*Black*	*Diffuse*	*BlackML*	*DiffuseML*	*Black*	*Diffuse*	*BlackML*	*DiffuseML*
10 mm	38.3	27.6	38.1	25.7	10.1	8.6	10.3	8.2
13 mm	48.6	34.1	42.3	33.3	9.7	8.3	9.4	7.8
17 mm	61.5	41.6	51.2	46.9	9.2	8.0	8.5	7.4
22 mm	71.8	58.1	74.2	59.3	8.7	7.8	7.8	7.1

Table 8. Percent contrast and percent background variability for the whole-body LSO TOF-PET scanner with time resolution of 150 ps included.

Sphere Size	Percent contrast ($Q_{H,j}$) (%)	Percent background variability (N_j) (%)
10 mm	29.0	7.9
13 mm	33.7	7.6
17 mm	42.8	7.3
22 mm	58.9	7.1

Table 9. Root mean square error for each optical surface treatment for the whole-body PbF_2 Cherenkov TOF-PET scanners with 100 ps time spread for the SiPMs and for the whole-body LSO TOF-PET scanner with time resolution of 150 ps included.

	Root mean square error (RMSE) ($\times 10^{-10}$)			
LSO	*Black*	*Diffuse*	*BlackML*	*DiffuseML*
3.84	3.18	5.76	2.91	4.72

Table 10. Structural similarity index metric of hot spheres for each optical surface treatment for the whole-body PbF_2 Cherenkov TOF-PET scanners with 100 ps time spread for the SiPMs and for the whole-body LSO TOF-PET scanner with time resolution of 150 ps included.

	Structural similarity index metric (SSIM)				
Sphere Size	LSO	*Black*	*Diffuse*	*BlackML*	*DiffuseML*
10 mm	0.55	0.79	0.44	0.66	0.50
13 mm	0.59	0.80	0.54	0.58	0.52
17 mm	0.61	0.86	0.71	0.73	0.76
22 mm	0.79	0.85	0.78	0.88	0.80

15 mm long PbF_2 crystals and *black* optical surface treatment a TOF resolution of 154 ps was achieved, which worsened to 196 ps in case of *diffuse* optical surface treatment. Nevertheless, using as a wrapping for the crystals the *diffuse* optical surface treatment much higher coincidence detection efficiency was achieved (5.7% compared to 1.5% using *black* optical surface treatment, for 15 mm long crystals and real photodetector parameters), which also resulted in better FOM. However, the FOM values depend on the FWHM of the TOF distribution and do not take into account the contribution of the long tails in TOF, which are the result of random reflections from the *diffuse* optical surface treatment. This became apparent when comparing the quantitative metrics of image quality: CNR, NEMA percent contrast, RMSE and SSIM values were better using *black* optical surface treatment than *diffuse* optical surface treatment.

The simulation results obtained with the multi-layer detector show that using such geometry the TOF resolution can be further improved without any sacrifices in the efficiency. When no SiPM time spread was included in the simulation, a 22 ps TOF resolution was achieved with the multi-layer detector and *black* optical surface treatment, indicating that with this configuration the main limitation remaining is the photodetector. The final results for the TOF of different configurations of a possible whole-body PbF_2 Cherenkov TOF-PET scanner are dominated by the time spread of the SiPMs but still better than the TOF resolution of the state of the art scanner using LSO crystals. An excellent TOF resolution of 29 ps was also achieved using the *diffuse* optical surface, however with the long tails due to random reflections. Also in the case of multi-layer geometry, the image quality using *diffuse* optical surface treatment was lower than with *black* optical surface treatment.

The image quality comparisons in this work were based on images reconstructed using MLP algorithms that have been shown to be comparable to more advanced algorithms for TOF resolution better than 100 ps (Vandenberghe and Karp 2006). For this reason the comparison may not be completely fair for the whole-body LSO TOF-PET scanner with TOF resolution of 223 ps, but using more sophisticated reconstruction algorithms better images could also be obtained for the whole-body PbF_2 Cherenkov TOF-PET scanners, especially when 100 ps of time spread for the SiPMs is included. We will further explore the extent of this by using iterative reconstruction algorithms provided by a Customizable and Advanced Software for Tomographic Reconstruction (CASToR) (Merlin *et al* 2018) in future work. Also important for the image quality comparison is the choice of the phantom size. The phantom simulated with a radius of 100 mm can represent a patient of 40 kg (Karp *et al* 2008). For larger phantoms (heavier patients) an even larger gain can be expected for TOF-PET scanner configurations with better TOF (Karp *et al* 2008).

The results obtained in this work are in good agreement with previously published studies of Cherenkov TOF-PET. In Alokhina *et al* (2018) a whole-body PbF_2 Cherenkov TOF-PET scanner was also simulated. Despite some differences in scanner and crystal dimensions, results very similar to this work were obtained: a TOF resolution of 180 ps using diffuse white coating treatment, compared to 196 ps for the *diffuse* optical surface simulated here. In case of black coating treatment compatible with the *black* optical surface treatment used in this work, a TOF of less that 40 ps was reported, compared to 61 ps obtained with 15 mm long PbF_2 crystals in this study. The differences can be mainly attributed to the photodetector simulated in each study: PMTs with 80 ps in Alokhina *et al* (2018) compared to the SiPMs with 100 ps of time spread used in this work. However, the recommended optical surface for the crystals in Alokhina *et al* (2018) was the diffuse white coating treatment, since that study placed more importance in the detection efficiency than in TOF resolution. In our case, better TOF and absence of long tails in TOF distribution lead to better quantitative image quality in case of *black* optical surface treatment.

5. Conclusion

A Cherenkov TOF-PET scanner can really push TOF improvements for PET devices, as it was shown in this study with the multi-layer geometry using *black* optical surface treatment, with which an intrinsic TOF of 22 ps was achieved. This represents the fundamental limitation for the TOF resolution of the simulated Cherenkov PET due to gamma stopping power, light production and light propagation to photodetector, but excluding the time spread for the photodetector, where the technology has not yet reached theoretical limits. With a realistic photodetector timing included in the simulation, the images obtained with a whole-body PbF_2 Cherenkov TOF-PET scanners are competitive to the image obtained with a whole-body LSO TOF-PET scanner, for all the different image quality metrics used. We are working on reconstructing the data presented here with more advanced algorithms, incorporating the effects of the SiPM dark counts in the simulation and on the experimental verification of the multi-layer detector performance. It is important to point out that to achieve the same gamma stopping power, smaller volume of crystals is needed for PbF_2 scanner than for LSO scanner, which in addition to the lower expected price of PbF_2 compared to traditional scintillators (Mao *et al* 2010) means reduced price of the scanners. The shorter crystals also reduce parallax error, which in combination with expected lower price and excellent TOF makes PbF_2 Cherenkov TOF-PET an attractive option for total-body TOF-PET scanner.

Acknowledgments

The authors acknowledge the financial support from the Slovenian Research Agency (research core funding No. P1-0135 and project J2-1735).

References

Allison J *et al* 2016 Recent developments in GEANT4 *Nucl. Instrum Methods* A **835** 186–225
Alokhina M, Canot C, Bezshyyko O, Kadenko I, Tauzin G, Yvon D and Sharyy V 2018 Simulation and optimization of Cherenkov TOF whole-body PET *Nucl. Instrum Methods* A **912** 378–81
Badawi R D *et al* 2019 First human imaging studies with the EXPLORER total-body PET scanner *J. Nucl. Med.* **60** 299–303
Budinger T F 1983 Time-of-flight positron emission tomography: status relative to conventional PET *J. Nucl. Med.* **24** 73–8
Cherry S R, Jones T, Karp J S, Qi J, Moses W W and Badawi R D 2018 Total-body PET: maximizing sensitivity to create new opportunities for clinical research and patient care *J. Nucl. Med.* **59** 3–12
Cherry S R, Sorenson J A and Phelps M E 2003 *Physics in Nuclear Medicine* (St. Louis: W B Saunders Co Ltd)
Conti M, Eriksson L, Rothfuss H and Melcher C L 2009 Comparison of fast scintillators with TOF PET potential *IEEE Trans. Nucl. Sci.* **56** 926–33
Dolenec R, Korpar S, Križan P, Pestotnik R and Verdel N 2016 The performance of silicon photomultipliers in Cherenkov TOF PET *IEEE Trans. Nucl. Sci.* **63** 2478–81
Hamamatsu Catalogue: S13361–3050 series MPPC Arrays (Cat. No.KAPD1054E02 Nov. 2018 DN)
Hsu D F C, Ilan E, Peterson W T, Uribe J, Lubberink M and Levin C S 2017 Studies of a next generation silicon-photomultiplier-based time-of-flight PET/CT system *J. Nucl. Med.* **58** 1511–8
Karp J S, Surti S, Daube-Witherspoon M E and Muehllehner G 2008 Benefit of time-of-flight in PET: experimental and clinical results *J. Nucl. Med.* **49** 462–70
Korpar S, Dolenec R, Križan P, Pestotnik R and Stanovnik A 2011 Study of TOF PET using Cherenkov light *Nucl. Instrum. Methods* A **654** 532–8
Lecoq P, Auffray E, Brunner S, Hillemanns H, Jarron P, Knapitsch A, Meyer T and Powolny F 2010 Factors influencing time resolution of scintillators and ways to improve them *IEEE Trans. Nucl. Sci.* **57** 2411–6
Mao R, Zhang L and Zhu R-Y 2010 A search for scintillation in doped cubic lead fluoride crystals *IEEE Trans. Nucl. Sci.* **57** 3841–5
Merlin T, Stute S, Benoit D, Bert J, Carlier T, Comtat C, Filipovic M, Lamare F and Visvikis D 2018 CASToR: a generic data organization and processing code framework for multi-modal and multi-dimensional tomographic reconstruction *Phys. Med. Biol.* **63** 185005
Miyata M, Tomita H, Watanabe K, Kawarabayashi J and Iguchi T 2006 Development of TOF-PET using Cherenkov radiation *Nucl. Technol.* **43** 339–43

Ooba T, Fukushima T, Kawai H, Konishi M, Nakayama H, Tabata M, Adachi I, Nishida S, Kishimoto H and Yokogawa H 2004 Proposal of Cherenkov TOFPET with silica aerogel *IEEE Nuclear Science Symp. Conf.* vol 6 pp 3781–4

Siemens Biograph Vision Technical Sheet, retrieved April 2019 www.siemens-healthineers.com

Strul D, Santin G, Lazaro D, Bretonad V and Morel C 2003 GATE (Geant4 application for tomographic emission): a PET/SPECT general-purpose simulation platform *Nucl. Phys.* B **125** 75–9

ter Weele D N, Schaart D R and Dorenbos P 2014 Intrinsic scintillation pulse shape measurements by means of picosecond x-ray excitation for fast timing applications *Nucl. Instrum. Methods* A **767** 206–11

Tomitani T 1981 Image reconstruction and noise evaluation in photon time-of-flight assisted positron emission tomography *IEEE Trans. Nucl. Sci.* **28** 4581–9

Vandenberghe S and Karp J 2006 Rebinning and reconstruction techniques for 3D TOF-PET *Nucl. Instrum. Methods* A **569** 421–4

Vereos Digital PET/CT Performance whitepaper, retreived April 2019 www.philips.com

Wang Z, Bovik A C, Sheikh H R and Simoncelli E P 2004 Image quality assessment: from error visibility to structural similarity *IEEE Trans. Image Process.* **13** 600–14